

Holographic Manipulation of Nanostructured Fiber Optics Enables Spatially-Resolved, Reconfigurable Optical Control of Plasmonic Local Field Enhancement and SERS

Liam Collard,* Filippo Pisano, Di Zheng, Antonio Balena, Muhammad Fayyaz Kashif, Marco Pisanello, Antonella D'Orazio, Liset M de la Prida, Cristian Ciraci, Marco Grande, Massimo De Vittorio,* and Ferruccio Pisanello*

Integration of plasmonic structures on step-index optical fibers is attracting interest for both applications and fundamental studies. However, the possibility to dynamically control the coupling between the guided light fields and the plasmonic resonances is hindered by the turbidity of light propagation in multimode fibers (MMFs). This pivotal point strongly limits the range of studies that can benefit from nanostructured fiber optics. Fortunately, harnessing the interaction between plasmonic modes on the fiber tip and the full set of guided modes can bring this technology to a next generation progress. Here, the intrinsic wealth of information of guided modes is exploited to spatiotemporally control the plasmonic resonances of the coupled system. This concept is shown by employing dynamic phase modulation to structure both the response of plasmonic MMFs on the plasmonic facet and their response in the corresponding Fourier plane, achieving spatial selective field enhancement and direct control of the probe's work point in the dispersion diagram. Such a conceptual leap would transform the biomedical applications of holographic endoscopic imaging by integrating new sensing and manipulation capabilities.


versatile, miniaturized, and inherently light-coupled.^[8] This has enabled a set of applications including enhanced sensing,^[9] near-field optical microscopy,^[10] high-efficiency second-harmonic generation,^[11] plasmonic lab-on-fiber,^[12,13] and integrated phase shift/beam steering.^[14] However, in achieving the highly attractive platform of fiber-based plasmonics, researchers face two distinct but strongly connected challenges. First, a nanofabrication challenge: integrating nanostructures on the fiber tip; second, a photonic problem: engineer the interaction between the plasmonic structures and the modal patterns of light propagation in single mode (SMFs) or multimode fibers (MMFs). In particular, due to modal interference, MMFs add an additional layer of complexity as coherent input light is scrambled, making them a turbid optical medium.

1. Introduction

Fueled by intriguing insights on fundamental nano-optical phenomena as well as by the wide variety of applications, plasmonic nanostructures enjoy a long-lived research interest.^[1–7] In this regard, fiber optics have naturally emerged as a desirable substrate for many applications as they are affordable,

The fabrication challenge is being tackled with a number of strategies including self-assembly,^[15] solid-state dewetting,^[12] nanolithographic methods,^[16] or focused ion beam nanomachining.^[14,17] The photonic problem has been frequently circumvented working on SMFs^[18] or by generating localized surface plasmon resonances (LSPRs) in nanoparticles or nanogaps, which are less sensitive to the modal complexity

L. Collard, F. Pisano, D. Zheng, A. Balena, M. Pisanello, C. Ciraci, M. De Vittorio, F. Pisanello
Center for Biomolecular Nanotechnologies
Istituto Italiano di Tecnologia
Arnesano LE 73010, Italy
E-mail: liam.collard@iit.it; massimo.devittorio@iit.it; ferruccio.pisanello@iit.it

 The ORCID identification number(s) for the author(s) of this article can be found under <https://doi.org/10.1002/smll.202200975>.

© 2022 The Authors. Small published by Wiley-VCH GmbH. This is an open access article under the terms of the Creative Commons Attribution-NonCommercial License, which permits use, distribution and reproduction in any medium, provided the original work is properly cited and is not used for commercial purposes.

DOI: 10.1002/smll.202200975

M. F. Kashif, A. D'Orazio, M. Grande
Dipartimento di Ingegneria Elettrica e dell'Informazione
Politecnico di Bari
Bari 70125, Italy
L. M. de la Prida
Instituto Cajal
CSIC
Ave Doctor Arce, Madrid 28002, Spain
M. De Vittorio
Dipartimento di Ingegneria Dell'Innovazione
Università del Salento
Lecce 73100, Italy

of light propagation in MMFs.^[13] At the same time, several groups excited surface plasmon resonances (SPRs) with a momentum matching strategy between the guided wave-vector and a periodic structure, or a metasurface, integrated on the fiber tip.^[14,19,20] Despite these advances, achieving full control over the photonic properties of the system as-a-whole remains unsolved.

In this work, we propose leveraging the wealth of information encoded in the modal propagation in multimode optical fibers to achieve reconfigurable control on spatiotemporal patterns of plasmonic resonances. We employed a wavefront shaping technique^[21–29] to reveal the links between the input light fields and the coupling mechanism of the turbid plasmonic-MMF. In particular, we used holography to control the SPR and LSPR response of two different types of nanostructures on the fiber tip: periodic arrays and nanoislands, dynamically manipulating their response in terms of intensity distribution patterns and radiative angles. Periodic nanostructures are known to give well defined plasmonic resonances making them ideal candidates for extraordinary optical transmission (EOT)^[1] whereas nanoislands have been reported to induce high enhancement factors for surface enhanced Raman spectroscopy (SERS).^[30] While Fourier plane manipulation gives a direct control to define the work point in the dispersion diagram,^[31] operating on local intensity allows for a highly confined activation of a specific subregion of the plasmonic facet, self-optimized spatially-resolved EOT, light focusing beyond the limit of the fiber NA and spatially-resolved SERS in a probe ready for endoscopic applications. The latter perspective is a tempting paradigm to exploit light-matter interactions for a range of biomedical applications.^[32] For example, the emerging use of endoscopic MMFs probes and plasmonic fiber optics in brain research promises new strategies to modulate neural activity and to probe the biochemical state of nerve cells.^[33,34] At the same time, we believe our work will open new possibilities to investigate the fundamental aspects on how guided modes interact with complex nanophotonic turbid media.^[35]

2. Results

2.1. Holographic Control of Plasmonic Resonances Through MMF

The optical system for holographically controlling the plasmonic distal facet of the MMF is displayed in **Figure 1A**. It is designed to operate on both the plasmonic output facet and the Fourier plane transmission, and to collect inelastically back-scattered photons, allowing to take advantage of the diverse responses of the different types of plasmonic structures realized on the fiber facet. A 633 nm laser beam was expanded to overfill the screen of a phase-only spatial light modulator (SLM) conjugated with the back aperture of a microscope objective (MO1) in order to focus the modulated wavefront on the input fiber facet (0.22 NA, 50 μm core diameter, ≈5 cm long). This fiber length was selected due to its compatibility with our nanofabrication systems. The input facet was monitored using an imaging path with a detector on the proximal end, CCD1. The plasmonic modes arising at the structured facet were monitored

using objective MO2 and two detectors: CCD-FI (facet image), optically conjugated with the plasmonic facet and CCD-FP, recording its Fourier plane response. Importantly, the optical train includes an endoscopic detection path for SERS measurements. To do this, the 633 nm excitation was directed to the fiber with a long pass dichroic mirror (DC), and the proximal facet was optically conjugated with a fiber bundle connected to a spectrometer, after discriminating the SERS signal from the laser pump with a notch filter (NF).

Using this system, we measured the plasmonic modes excited on the distal end of the plasmonic MMF when applying a set of phase-modulated input light fields on the proximal end of the fiber. In the following, we define as (x_{in}, y_{in}) (or (x_{out}, y_{out})) the spatial coordinates in the image plane of the input (or output) facet and (u_{in}, v_{in}) (or (u_{out}, v_{out})) as the spatial coordinates in the Fourier plane of the input (or output) facet. The SLM was set to generate two combined sawtooth phase gratings $\phi_{interfere}^{j_x, j_y, p}(x_{in}, y_{in}) = \arg(\exp(i\phi_{scan}^{j_x, j_y, p}(x_{in}, y_{in})) + \exp(i\phi_{ref}))$ in the Fourier plane of the input facet in order to produce: i) a reference beam B_{ref} generated by the grating $\phi_{ref}(u_{in}, v_{in})$, which passed at the center of the fiber core, and ii) a scanning beam B_{scan} that sequentially impinged on a 25 by 25 array of spots (indexed by j_x and j_y) on the proximal facet of the fiber (image plane) with phase p ranging from 0 to 2π , considering the indexing, every scanned spot on the input facet was indexed as $B_{scan}^{j_x, j_y, p}$ and was generated by the grating $\phi_{scan}^{j_x, j_y, p}(u_{in}, v_{in})$ (Figure 1B). We chose to use a common optical path with an internal reference beam passing through the MMF to increase the interferometric stability of the calibration procedure. In this way, the propagation of $B_{scan}^{j_x, j_y, p}$ and B_{ref} through the multimode fiber generated an interference pattern that, in turn, excited plasmonic modes on the output facet, which were then reflected in the light field structuring in both (x_{out}, y_{out}) and (u_{out}, v_{out}) planes (CCD-FI and CCD-FP, in practical terms). The phase shift $p_{opt}^{j_x, j_y}$ generating the maximum intensity at the targeted output pixel was stored. Thus, for each point in the plasmonic output facet or in the output Fourier plane a phase modulation pattern was generated maximizing the intensity at each targeted pixel

$$\Phi(u_{in}, v_{in}) = \arg\left(\sum_{j_x=1}^{25} \sum_{j_y=1}^{25} \exp\left(i\phi_{scan}^{j_x, j_y, p_{opt}^{j_x, j_y}}(u_{in}, v_{in})\right)\right) \quad (1)$$

The full details of this procedure are reported in the Experimental Section.

This method provides the effective modulation of the input beam in order to hold the working point of the system, either on the plasmonic output facet or the Fourier plane, regardless of the morphology of the resonant substrate, with the temporal control limited only by the refresh rate of the SLM. To demonstrate its versatility, we employed our approach with plasmonic-MMFs hosting three different types of plasmonic structures for three different goals (Figure 1C): a) spatially resolved EOT through subportions of plasmonic nanoholes arrays with varying periodicity on the same MMF, b) dispersion diagram engineering through orthogonal plasmonic nanograting on the same MMF, c) Spatially resolved SERS through an MMF facilitated by nanoislands at the fiber tip.

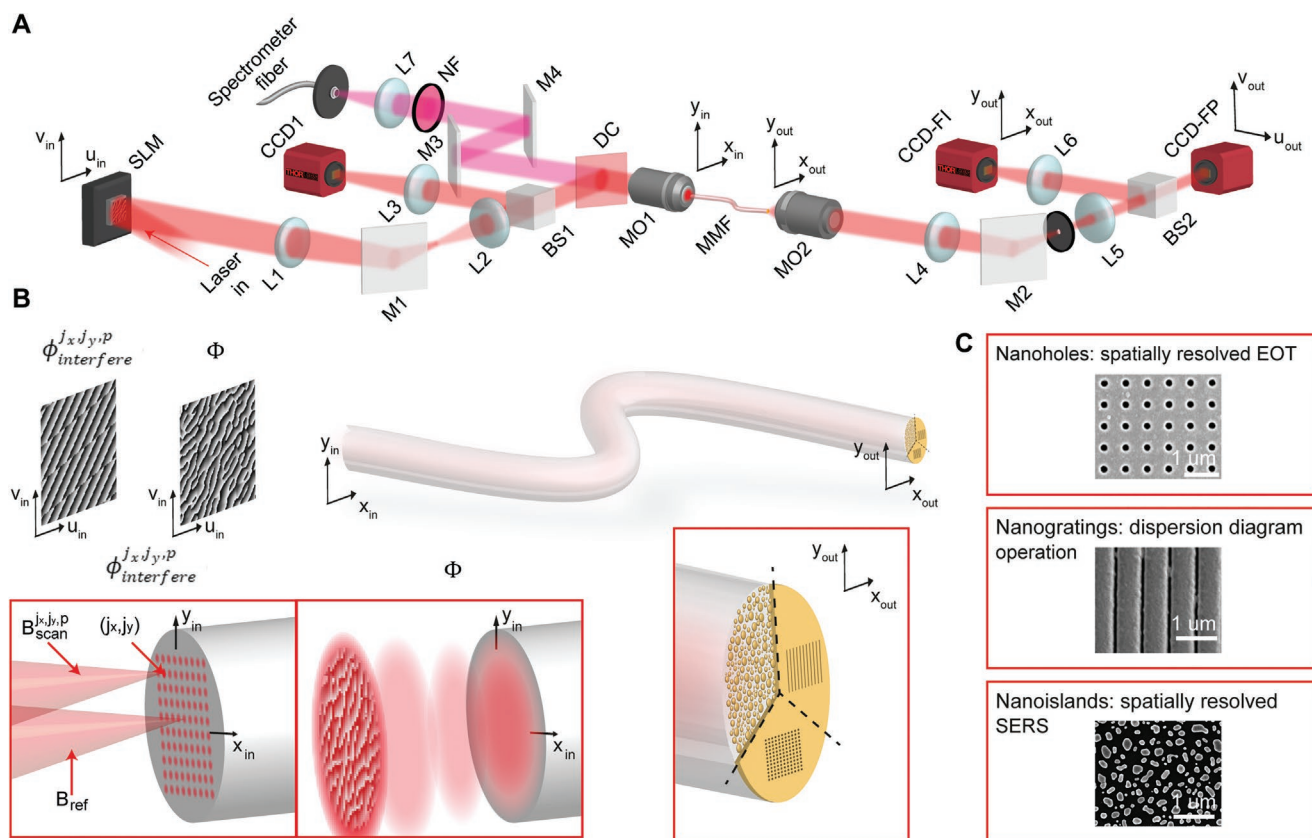


Figure 1. System for holographic control of coupling between plasmonic resonances and guided modes in multimode fibers. A) Implemented optical system: SLM—spatial light modulator, L—lens, M, mirror, BS—beam splitter, CCD—charged coupling device, DC—dichroic mirror, MO—microscope objective, MMF—multimode fiber (≈ 5 cm long), PH—pinhole, NF notch filter. B) Example of wavefront phase modulation to holographically control the distal, nanostructured fiber facet. $\phi_{interfere}^{j_x, j_y, p}(x_{in}, y_{in}) = \arg(\exp(i\phi_{scan}^{j_x, j_y, p}(x_{in}, y_{in})) + \exp(i\phi_{ref}))$ was used to generate an interference pattern between B_{ref} and $B_{scan}^{j_x, j_y, p}$, while $\Phi(u_{in}, v_{in})$ generated the effective modulation (details reported in the methods section). C) SEM images of nanohole arrays, nanogratings, and nanoislands realized on MMF's facet.

The details of these applications are reported in the following, dedicated sections.

2.2. Spatiotemporal Control the Plasmonic Resonances in the Coupled System

We implemented the holographic procedure described above to scan a highly localized spot across nine different arrays of nanoholes, 100 nm in diameter (Figure 2A) realized on the fiber facet with Focused Ion Beam lithography at low currents^[36] (see the Experimental Section). The nanohole arrays were arranged in a 3×3 matrix and had periodicities ranging from 560 to 720 nm with a 20 nm step (increasing from left to right and top to bottom), as shown in Figure 2B. To investigate the highest number of periodicities on a single fiber while ensuring the nanostructures were larger than a diffraction limited focus generated by the fiber, each nanohole array was $7.5 \times 7.5 \mu\text{m}^2$ large (about twice the diffraction limit of 0.22 NA optics). Video S1 (Supporting Information) shows the focal spot scanning across the nine different nanoholes arrays, while nine representative frames from Video S1 (Supporting Information) are shown in Figure 2C, with a single spot exciting each of the nine structures and the complete set of spots displayed in

the overlay diagram in Figure 2D. These results show that the wavefront engineering approach enables the optical transmission to be localized through a few nanoholes (from 20 to 35 in this experiment) by exploiting the modal diversity of the MMF (the temporal resolution is given by the refresh rate of the SLM (50 ms). At the same time, they carry insights on the field profile in the image and Fourier plane of the output facet.

In the (x_{out}, y_{out}) plane, the localized spots have an average waist along x_{out} and y_{out} of $w = 3.4 \pm 0.7 \mu\text{m}$, with the related histograms reported in Figure 2E,F. When compared against the fiber NA, the beam width w demonstrates that our method reaches the diffraction limit of the MMF given by $d = \frac{1.21\lambda}{NA} = \frac{1.22 \times 633 \text{ nm}}{0.22} = 3.5 \mu\text{m}$ (the resolution of the detec-

tion arm is given by $r = \frac{\lambda}{2NA} = 1.055 \mu\text{m}$). Such a configuration will hopefully permit recordings at subcellular resolution when applied to biological samples, a key challenge for endoscopic applications.

We investigated if the localized spots have subdiffraction features by increasing the NA of MO2 to 0.65 (in this case 4 nanohole arrays were milled on the fiber facet). A characteristic example of the obtained image of localized intensity spot is shown in Figure 2G,H and the related finite-difference

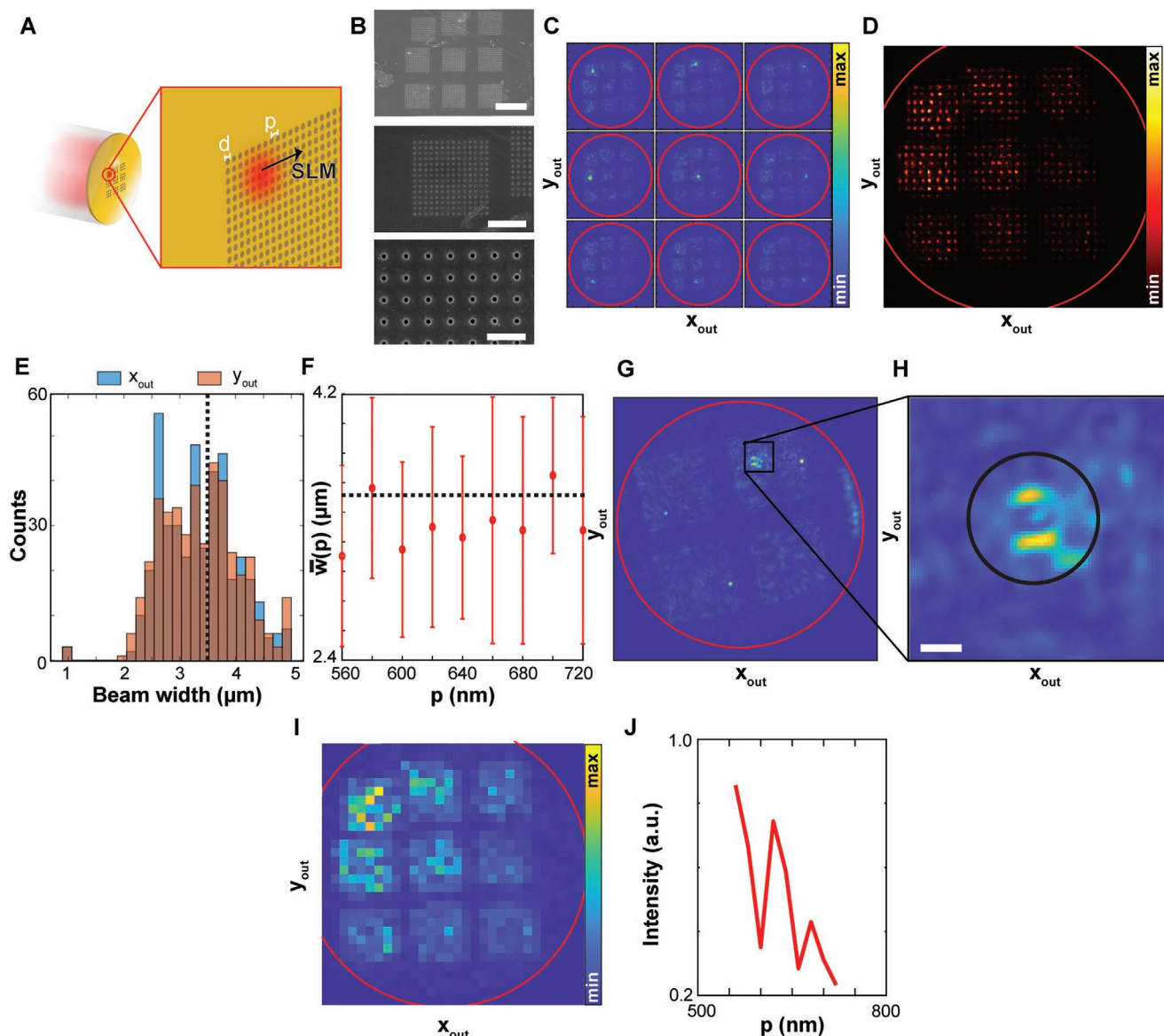


Figure 2. Spatially-resolved extraordinary optical transmission. A) Illustration of nanoholes' fiber design. B) SEM images of nanohole arrays milled on the fiber facet. Scale bars represent 10, 4, and 1 μm respectively (top to bottom). C) Holographically shaped spots through each of the nine nanohole arrays. D) Overlay of 30 by 30 array of spots generated over the distal facet of the fiber. E) Histogram of waists w for each wavefront-shaped spot. F) Average of $w(p)$ for each of the nine nanohole arrays. Error bars represent standard deviation on between 20 and 30 spots for each value of p . G, H) Evidence of subdiffraction limit features through a nanohole array milled fiber (scale bar in panel I represents 1 μm and the black circle represents the theoretical diffraction limit). I) Maximum value of intensity for each spot generated through the nanoholes. J) Average maximum intensity on each nanohole array. In panels (C), (D), (G), and (I) the red circles represents the fiber facet, whose diameter is 50 μm .

time-domain (FDTD) simulations are shown in Figure S1 (Supporting Information). In the simulations, the intensity pattern shows similar subdiffraction features to the experiment.

A representative feature of EOT is the dependence of the transmitted intensity on local periodicity,^[1] as also confirmed by rigorous coupled-wave analysis (RCWA) in a numerical model reproducing our nanoholes arrays (see Figure S2A,B, Supporting Information). To experimentally confirm it, the maximum transmitted intensity for each of the 30×30 spots was recorded and displayed in Figure 2I, highlighting the modulation linked to different values of p . Thus, the holographic

approach allows the EOT of monochromatic light for each structure to be characterized. As the procedure maximizes the intensity at $(x_{\text{out}}, y_{\text{out}})$, the map in Figure 2I represents a direct measurement of the maximum transmission achievable at each specific point. The dependence of the transmittance as a function of p is displayed in Figure 2J, with transmission peaks at $p = 560, 620,$ and 680 nm.

This difference in transmission across structures can be therefore attributed to variable transmission efficiency based on the EOT through a few nanoholes of the arrays, since in nonstructured MMFs the intensity of the wavefront-shaped

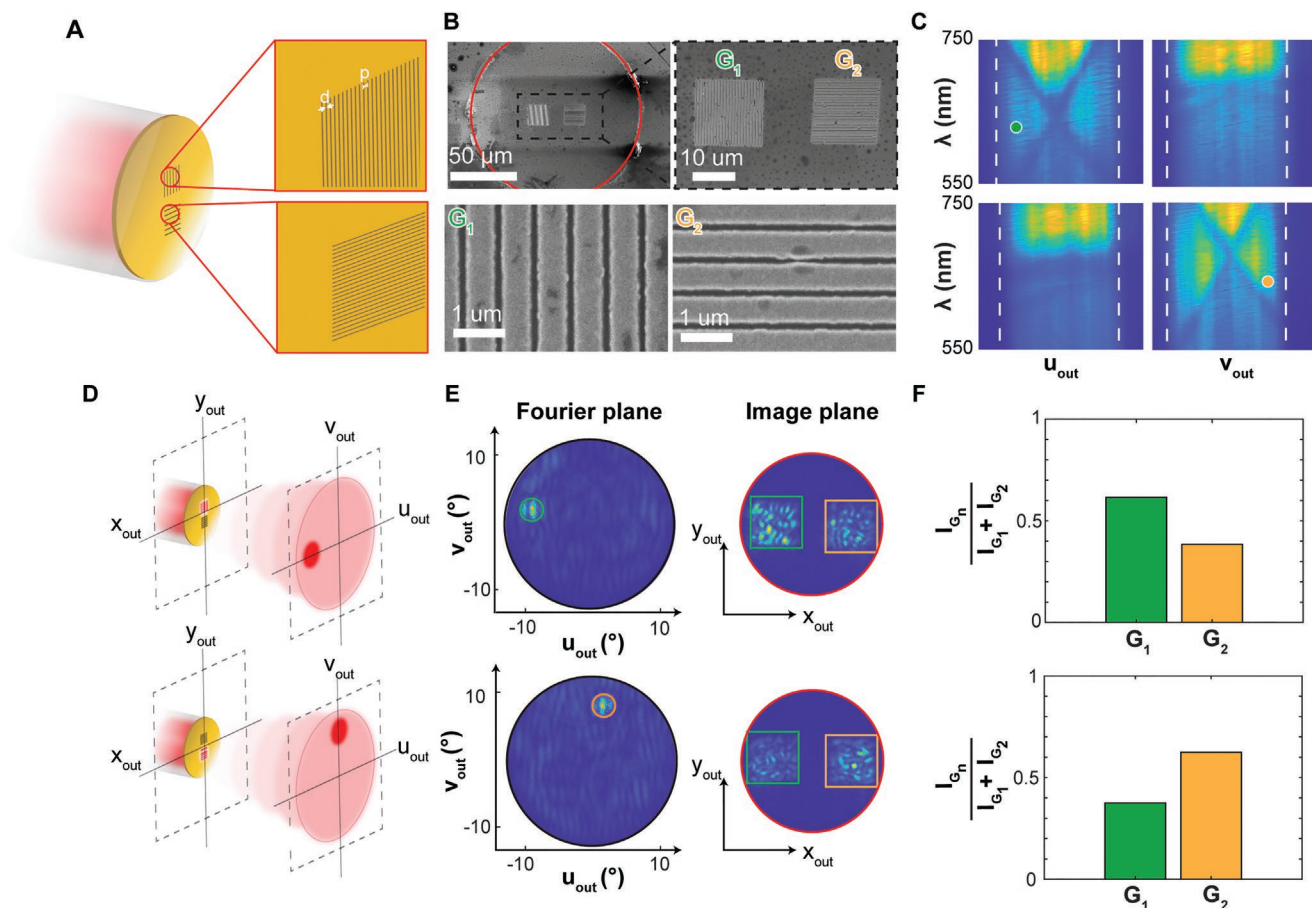


Figure 3. Setting the workpoint of the coupled system in the dispersion diagram A) Illustration of nanograting milled fiber design. B) SEM images of nanograting milled fiber. C) Experimentally observed dispersion diagrams from G1 (top row, with G2 blocked) and G2 (bottom row, with G1 blocked), along u_{out} (left) and v_{out} (right), the NA of the MMF is shown by the white dashed lines. The setup used to measure these dispersion diagrams is shown in Figure S5D, Supporting Information. D) Illustration of direct control of Fourier plane response of the multiresonant system using the holography approach. E) Holographically generated Fourier plane foci (left) and corresponding plasmonic facet intensity distribution (right). F) Total intensity confined within G1 and G2 for each of the orthogonal Fourier plane foci. Red circles in panels B and E represent the core diameter.

output foci only decreases close to the core cladding interface (see control experiment in Figure S3 and Video S2 (Supporting Information), where the transmission efficiency of the system is also analyzed). Together with the dependence on periodicity, an additional feature of nanoholes arrays is their angular-dependent response, shown in the Fourier plane ($u_{\text{out}}, v_{\text{out}}$) displayed in Figure S2C,D (Supporting Information).

The impact of the dimensions of the nanohole array on the focused spot size was also assessed. We generated scanning focused spots on four larger nanoholes arrays ($15 \times 15 \mu\text{m}^2$) with periodicity 610, 630, 640, and 660 nm, as shown in Figure S4A,B (Supporting Information). The width of spots is shown as histogram in Figure S4C (Supporting Information) and plotted against nanostructure periodicity in the inset. Also in this case, the spot size approaches the diffraction limit. Figure S4D (Supporting Information) compares the average sizes of 3.36 ± 0.53 and $3.59 \pm 0.52 \mu\text{m}$ (average spot diameter \pm standard deviation) for foci generated on the $7.5 \times 7.5 \mu\text{m}^2$ and $15 \times 15 \mu\text{m}^2$ structures, respectively. Thus, it can be inferred that, in this regime, the size of the localized spot does not depend on the dimensions of the periodic structure.

The structured Fourier plane responses of periodic plasmonic nanostructures can be considered as a control gate to their optical functionalities, for instance to target a specific location in the system's dispersion diagram. This can be accomplished using our method to select a specific point in the Fourier space of a multiresonant structure using a single wavelength source (Figure 3A). To show this, we fabricated a plasmonic MMF (0.22 NA) with two orthogonal, 1D, plasmonic, nanogratings: G1, with slits oriented parallel to y_{out} and G2, with slits parallel to x_{out} , SEM images of the nanostructured fiber facet are shown in Figure 3B. It should be noted that as well as scrambling the amplitude and phase of input light, the linear polarization of input light is also scrambled and thus, both nanogratings are capable of transmitting.

First, the transmission dispersion diagrams of the two structures were measured via Fourier microspectroscopy of broadband excitation^[35] (the experimental path is shown in Figure S5, Supporting Information). This was performed in two configurations: with the u_{out} axis of the Fourier plane aligned to the spectrometer slits, and then, by rotating the fiber by 90° , with the spectrometer slits aligned to the v_{out} axis. In each

configuration, each grating was selected by blocking the other with a razor blade. The resulting four dispersion diagrams are shown in Figure 3C (and in Figure S6, Supporting Information, in wavevector units). This measurement confirmed that G1 modulates the response along u_{out} , while G2 modulates along v_{out} . A strong angular-dependent resonance was observed when G2 is aligned with v_{out} or G1 is aligned with u_{out} (straight configuration). In the cross-configuration, i.e., with G2 aligned to u_{out} and G1 with v_{out} , a weakly modulated resonance is observed at approximately the same wavelengths observed for $u_{\text{out}} = 0$ or $v_{\text{out}} = 0$ in the straight configuration, reflecting the main modulation of the straight configuration on the opposite axis (see Figure S7, Supporting Information).

Using the holographic system, the fiber was forced to work at a specific point of the transmission dispersion diagram: the wavelength was fixed at 633 nm and specific wavevectors were selected by modulating its Fourier plane response, as illustrated in Figure 3D (i.e., generating Fourier plane foci on CCD-FP). Two orthogonal points in the dispersion diagrams (see green and yellow points in Figure 3C) were targeted generating focused spots at the related points in the $(u_{\text{out}}, v_{\text{out}})$ plane (Figure 3E), with the corresponding images of the plasmonic output facet shown on the right. As the Fourier plane foci were positioned along either the u_{out} or v_{out} axis, selecting the Fourier plane spot modulated the transmitted intensity in the image plane, boosting the grating that responds along the chosen axis. As shown in the bar charts in Figure 3F, the recruited grating had a 1.56 intensity increase, measured as I_{G1}/I_{G2} or I_{G2}/I_{G1} . It should be noted that the residual transmission on the inactivate nanograting corresponds to unmodulated light of the alternative polarization. This therefore suggests that despite the coupling between periodic nanostructures and guided modes would in principle be altered by the turbidity of the MMF, wavefront engineering can be applied to set and hold the workpoint of the system in the dispersion diagram, as commonly done in microscopy-based applications requiring a precise control of the excitation angle. In addition, we have provided a proof of principle that this approach allows leveraging modal effects to reconfigure the response of fiber-based multiresonant structures acting on the Fourier plane of transmitted light. While we have chosen a simple example using two spatially modulating 1D arrays, we believe this concept can be extended to more complex structures exploring a broader range of resonant parameters (e.g., wavelength, polarization, orbital angular momentum or a combination of them). In addition, recent reports shown that phase modulation can be employed for MMF Fourier plane endoscopy and would greatly benefit on the ability to exploit the effect of plasmonic resonances to structure the spatial and angular response of the imaging system to further multiplex signal acquisition.^[23,31]

2.3. Spatially-Resolved SERS Through a Plasmonic-MMF

As the holographic system can operate across the dispersion diagram, it is highly promising also for exploiting optical fibers featuring plasmonic nanostructures with transmission properties independent of the excitation angle and very broad resonances, such as self-assembled nanoislands (NI).^[12,30,32] To this

aim, we investigated the coupling between gold NIs and a MMF to realize a spatially-resolved SERS endoscope (Figure 4A). A solid-state dewetting approach was applied on a thin gold film deposited on the fiber facet (see the Experimental Section). Representative results of the fabrication process are shown in the SEM micrographs in Figure 4B, from which we assessed an average size of ≈ 150 nm and an average inter-islands distance, noted as effective gap, of ≈ 100 nm. The extinction spectra of the dewetted NIs fiber were measured with a transmission configuration exciting either the full fiber facet or 3 μm localized spots (Figure 4C) to demonstrate the uniformity of the resonance with respect to size and position of the excitation region. The NIs layer allows for high local field enhancement and serves as a highly active SERS substrate on the fiber facet.^[12] This was experimentally verified by comparing the Raman spectra recorded by direct excitation with a 633 nm laser on a monolayer of benzenethiol (BT) molecules functionalized NIs fiber and a control fiber coated with a thin layer of gold (Figure S8, Supporting Information). The BT molecule Raman peaks (at 983, 1007, 1059, and 1562 cm^{-1}) are enhanced by the NIs layer: between the gold thin film and NIs fiber an intensity ratio of 24.38 was observed for the 1562 cm^{-1} peak. The silica Raman spectra from the fiber is also attenuated by the NIs fiber and, to a greater extent, by the gold thin film (the attenuation is ≈ 2.3 times higher for the gold thin film).

To collect a spatially resolved SERS signal through the MMF, a 30×30 square array of points overlapping the NIs fiber distal facet functionalized with BT molecules was generated using the SLM. Video S3 (Supporting Information) shows a raster scanning of the localized spots across the plasmonic facet. The maximum intensity for each focus is reported in the color map in Figure 4D, while Figure 4E displays a histogram of the obtained waists (w): despite the scattering of the NIs introduces an additional layer of randomness to the turbidity of mode propagation in MMFs, we measured a waist of $w = 3.7 \pm 0.4 \mu\text{m}$, close to the diffraction limit of the 0.22 NA fiber (3.5 μm). The SERS signal was then collected through the fiber with the localized spots in different positions, as shown in Video S4 (Supporting Information) and in Figures 4F–H. Resulting spectra are a convolution of both the silica background from the fiber (with the main peak at 787 cm^{-1}) and the BT molecule SERS signal, with prominent peaks at 1059 and 1562 cm^{-1} , with both the silica and BT components of similar intensity. Recent reports have shown, that in the fingerprint region, the fiber background signal is between 10 and 50 times higher than that of polystyrene beads dried on the fiber tip.^[38] Indeed, for conventional Raman imaging through a MMF presently the high wavenumber region is preferred due to the lower background signal in this region. Our method demonstrates that by integration with plasmonic structures the fingerprint region can also be explored for spatially resolved SERS measurements, significantly improving the chemical specificity of the technique and have the potential of integrating molecular sensing in plasmonic neural endoscopes based on holographic imaging systems.^[39,40] As it has been shown that wavefront engineering can be used to control the output in longer MMFs with the respect to the here employed 5 cm length,^[41] we expect that longer waveguides can be employed also in the case of the here-described plasmonic plasmonic application.

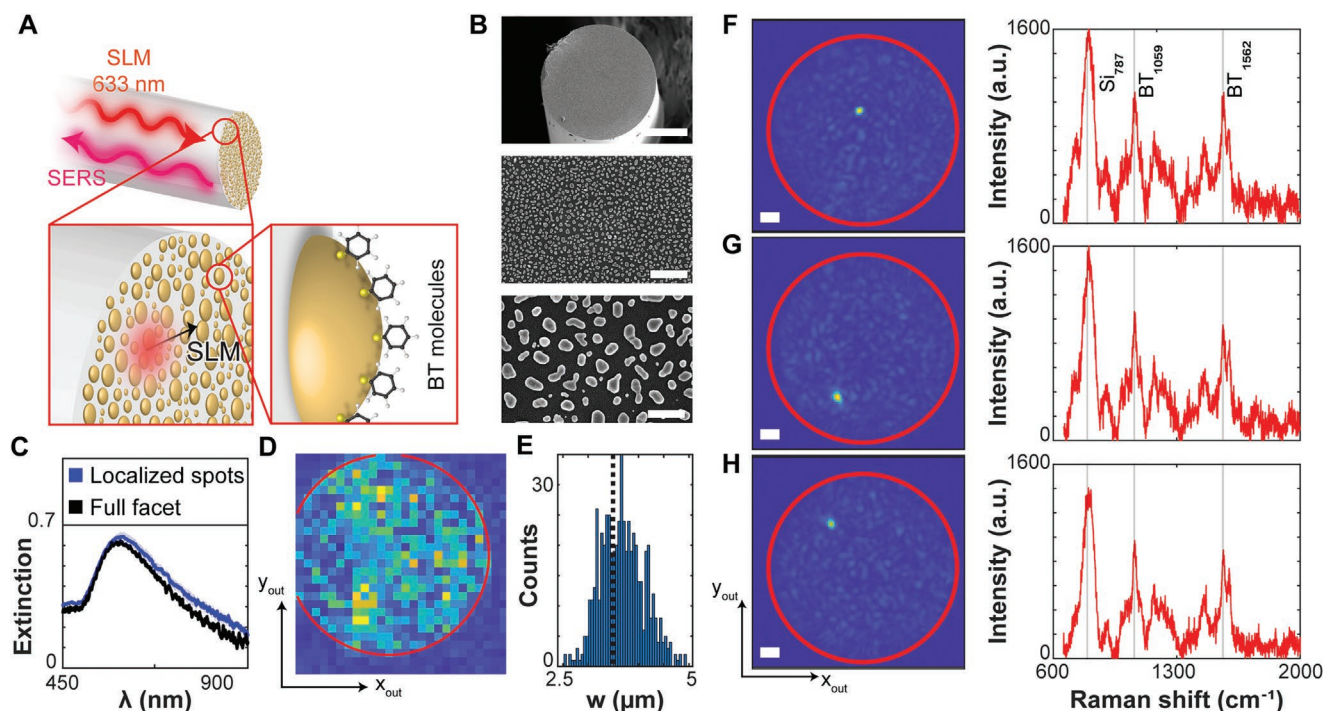


Figure 4. Spatially resolved surface enhanced Raman spectroscopy through a plasmonic MMF. A) Illustration of fiber design, inset focused spot generated through NIs fiber. B) SEM images of a of NIs fiber facet. scale bars 50, 2 μm , and 500 nm (top to bottom). C) Broadband transmission of a NIs fiber taken by collecting light from the entire facet (black) and from a micrometer-sized subregions (blue curve shows average over 5 different collection spots, while the shaded region represents standard deviation). D) Intensity of 30×30 array of focused spots generated through the fiber. E) Histogram of waists of the focused spots whose intensity is reported in panel D. F–H) SERS spectra of BT molecules (graphs on the right) taken by activating a subset of NIs on the fiber facet (transmission image shown on the left), the power was 1 mW at the proximal facet.

3. Discussion

We demonstrated that by employing wavefront shaping the modal diversity of MMFs can be exploited to control the coupling between guided modes and either periodic or random nanostructures, shaping both the intensity distribution and the angular response of the coupled system. All-optical manipulation of nanoscale light-matter interaction on the output facet of an optical fiber, in turn, lays the ground for fully integrated plasmonic endoscopes based on both EOT and SERS phenomenology, potentially hosting a diverse ensemble of activatable plasmonic structures. Holographic imaging methods have been applied for fluorescence imaging through MMFs in tissue^[42] and in living animals,^[39,40] controlling the coupling between guided modes in MMFs and plasmonic structures could potentially add molecular sensing capability, with techniques such as deep learning,^[22] guide star,^[24] side view fibers^[43] all able to improve the translatability of the approach.

In addition, recent reports have shown that the field of MMFs endoscopy can greatly benefit of Fourier plane-based approaches.^[23,31,44] In this respect, the complex coupling between periodic plasmonic structures and the MMF's randomness can be harnessed by defining and holding a specific work point on the dispersion diagram (Figure 3E), setting the stage for endoscopic approaches based on EOT. This concept is shown in this work in a fiber optic featuring two orthogonal plasmonic nanogratings, and could be extended to ideally any

type of photonic structures on the fiber facet, including dielectric metasurfaces.^[35,45]

In conclusion, we have shown that taking advantage of the modal diversity in MMF enables a set of applications that leverages on the peculiar properties of nanophotonic structures realized on the fiber facet. These results will inspire new applications of plasmonic-based endoscopy, including paving the way toward the integration of spatially-resolved molecular sensing and plasmonic beam shaping to target specific patterns in the Fourier plane.

4. Experimental Section

Optical Path: The implemented optical setup for performing holography through a MMF is displayed in Figure 1A. A 633 nm laser beam was expanded and its polarization was rotated with a half wave plate to match the screen of the SLM (ODP512, Meadowlark optics). Lenses L1 ($f_{L1} = 400$ mm) and L2 ($f_{L2} = 200$ mm) formed a 4f relay between the SLM and the back aperture of the microscope objective MO1 (0.65 NA, 40x, AMEP4625, ThermoFisher), which coupled light into the plasmonic MMF. BS1 (a 10:90 (R:T) beam splitter) was used to image the reflection of the input facet onto a camera (CCD1). Light transmitted through the plasmonic structures was collected by the microscope objective MO2 (10x, 0.3 NA, MPLFLN10x—Olympus, effective focal length $f_{MO2} = 18$ mm), except in the case of the high NA measurement of nanohole arrays (Figure 1G,H) in which case a 0.75 NA, 50x, MplanN, Olympus objective was employed. The back focal plane of MO2 formed a 4f system with lenses L4 ($f_{L4} = 125$ mm) and L5 ($f_{L5} = 100$ mm) and

CCD-FP (CS505MU—Thorlabs) so that the Fourier plane of the fiber is projected onto CCD-FP. A 50:50 beam splitter was placed after L5 and the plasmonic facet was imaged onto CCD-FI (CS505MU—Thorlabs) using lens L6 ($f_{L6} = 100$ mm).

SERS signal was collected through the plasmonic MMF and transmitted through a long-pass RazorEdge dichroic mirror (DC, Semrock, LPD02-633RU). A notch filter (NF, Semrock, NF03-633E-25) was used to remove residual excitation laser and the resulting signal was focused onto a round to linear fiber bundle using L7 ($f_{L7} = 50$ mm). The linear facet of the bundle was imaged on the entrance slit of a 320 mm focal length spectrometer (iHR320, Horiba). SERS and Raman measurements were performed with slits at 200 μm and a 600 lines per mm grating (blaze 750 nm). Spectra were recorded on a SYNAPSE CCD cooled to -50 $^{\circ}\text{C}$ with 30 s acquisition time.

Phase Modulation Procedure: The transmission of 633 nm light through plasmonic MMFs was shaped using the SLM driven by a custom-written matlab script. Prior to the calibration procedure, sawtooth gratings, $\phi_{\text{scan}}^{j_x, j_y, p}(u_{\text{in}}, v_{\text{in}}) = \text{mod}(au_{\text{in}} + bv_{\text{in}}, 2\pi)$ and $\phi_{\text{ref}}(u_{\text{in}}, v_{\text{in}}) = \text{mod}(c(u_{\text{in}} + v_{\text{in}}), 2\pi)$ were defined, where a and b set the periodicity of the grating along x_{in} , and y_{in} so the beam $B_{\text{scan}}^{j_x, j_y, p}$ scans a 25×25 grid on the input facet of the plasmonic MMF. c was chosen so that the reference beam B_{ref} was fixed at the center of the input facet of the plasmonic MMF. p represents the phase shift applied to the scanning points incremented in steps of $\frac{\pi}{2}$. Therefore, when the phase modulation pattern $\phi_{\text{interfere}}^{j_x, j_y, p}(u_{\text{in}}, v_{\text{in}}) = \text{arg}(\exp(i\phi_{\text{scan}}^{j_x, j_y, p}(u_{\text{in}}, v_{\text{in}})) + \exp(i\phi_{\text{ref}}))$ was applied to the SLM both $B_{\text{scan}}^{j_x, j_y, p}$ and B_{ref} were generated simultaneously. Interference patterns were therefore recorded on both CCD-FI and CCD-FP. By iterating on (j_x, j_y) , $B_{\text{scan}}^{j_x, j_y, p}$ was scanned across the input facet (Figure 1B), while keeping B_{ref} at the center of the core. For each (j_x, j_y) , p was shifted by increments of $\frac{\pi}{2}$ while monitoring the intensity on both $(x_{\text{out}}, y_{\text{out}})$ and $(u_{\text{out}}, v_{\text{out}})$ planes (between each phase modulation pattern sent to the SLM measurement was paused for 50 ms to allow the SLM to refresh). The phase shift $p_{\text{opt}}^{j_x, j_y}$ generating the maximum intensity at the targeted output pixel was stored. Thus, for each point of the plasmonic output facet or Fourier plane a phase modulation pattern was generated maximizing the intensity at each targeted pixel

$$\Phi(u_{\text{in}}, v_{\text{in}}) = \text{arg} \left(\sum_{j_x=1}^{25} \sum_{j_y=1}^{25} \exp \left(i \phi_{\text{scan}}^{j_x, j_y, p_{\text{opt}}^{j_x, j_y}}(u_{\text{in}}, v_{\text{in}}) \right) \right) \quad (2)$$

This computation was then completed on the graphics processing unit (GPU—NVIDIA GeForce GTX 960).

Fabrication of Periodic Nanostructures: Periodic nanostructures were patterned on the fiber tip using Focused Ion Beam milling (FEI DualBeamHeliosNanoLab600i). The fiber tip was connected to a metallic ferrule, polished and coated with an adhesion layer of chromium (5 nm) followed by a 130 nm layer of gold using thermal evaporation. Then, the fiber was mounted in the FIB chamber, with the metallic end facing the ion beam, using a custom mount. The metallic ferrule provided for electric continuity between the metal layer and the FIB holder. The periodic array of nanoholes and nanogratings were milled on the tip by sequentially scanning a Ga⁺ ion beam accelerated at 30 kV, at 7.7 pA current (nominal beam size 9.8 nm), with 1 μs dwell time and minimal overlap (5–10%).^[36] The patterns were designed with commercial software (FEI NanoBuilder).

Nanoislands Fabrication: Multimode silica optical fibers (Thorlabs, FG050UGA, 0.22 NA, $\varnothing 50$ μm Core) were used for the sample fabrication. First, fibers with fixed length (7.5 cm) were put in an acetone bath for 30 min to remove the acrylate jacket. Then, a manual fiber cleaver (Thorlabs, XL411) was used to cut one side of the fiber to obtain a flat distal fiber facet. Cleaved optical fibers were then fixed on a custom built batch mount printed with 3D printer (Ultimaker S3) to align the top surfaces of the fibers normal to the Au source in a crucible of an e-beam evaporator (Thermionics laboratory, inc. e-GunTM). A thin Au film was evaporated on the fiber-top surfaces with a deposition rate of 0.2 \AA s^{-1} under the chamber pressure of 6×10^{-6} mbar. Subsequently, the fibers were detached from the mount and arranged in a ceramic

bowl without any adhesive for thermal annealing in a muffle furnace (Nabertherm B180). The furnace gradually ramped the temperature from room temperature (RT) to 600 $^{\circ}\text{C}$ with a rate of 10 $^{\circ}\text{C min}^{-1}$, and held at 600 $^{\circ}\text{C}$ for 1 h, after which, it was allowed to cool ambiently to RT, yielding nanoislands (NIs) fibers.

Simulations: 3D simulation models of the periodic nanostructures using finite-difference time-domain (FDTD) and rigorous coupled-wave analysis (RCWA) methods for numerical investigations were realized. Commercially available codes were used from Rsoft for these simulations. For gold, a Drude–Lorentz model was used given by the following equation

$$\epsilon_m(\omega) = \epsilon_{\infty} - \frac{\omega_D^2}{\omega^2 + j\omega\gamma_D} - \sum_{k=1}^2 \frac{\delta_k \omega_k^2}{\omega^2 - \omega_k^2 + 2j\omega\gamma_k} \quad (3)$$

where ϵ_{∞} is metal dielectric constant at the high frequency regime in the Drude model, ω_D and γ_D are the plasma and collisions frequencies of free electron gas related to Drude model, whereas δ_k , ω_k , and γ_k , $k = 1, 2$, are amplitude, resonant angular frequency, and damping constant of each Lorentz-like oscillator, respectively.

To calculate transmittance from nanohole array, a 3D RCWA model of a nanohole was used on glass substrate where a plane wave excitation with periodic boundary conditions is used. RCWA method is most suitable for simulating periodic structures with plane wave excitations. For near field calculations from the nanoholes, Gaussian wave excitation instead to match the experimental spot size was used. This was achieved by using a 3D FDTD model of the finite structure with PML boundaries.

Nanoisland Substrate Relative Enhancement Factor. The substrate relative enhancement factor is defined as $SREF = I_{\text{NI}}/I_{\text{TF}} \times SC_{\text{TF}}/SC_{\text{NI}}$, where I_{NI} and I_{TF} are the intensity of the spectral line under consideration for the nanoisland (NI) and thin film (TF) fibers, respectively.^[46] SC_{TF} and SC_{NI} are instead the surface covered by the thin film (e.g., the entire fiber core) and by the nanoislands. For the experiment described in Figure S8 (Supporting Information), considering the 1562 cm^{-1} spectral line $SREF$ was estimated to be $SREF \approx 80.6$.

Statistical Analysis: In all data analysis, error bars were the standard deviation of the data set. All calibration generated 900 foci (in a 30×30 array) and only foci on the fiber facet or on plasmonic structures were analyzed further. The spot size was measured as the full width at $1/e^2$ and the intensity was taken as the maximum. The polynomial baseline was removed from the Raman/SERS spectra by alternating least squares fitting. All data were analyzed using MATLAB.

Supporting Information

Supporting Information is available from the Wiley Online Library or from the author.

Acknowledgements

L.C. and Fi.P. contributed equally to this work. M.D.V. and Fe.P. jointly supervised and are co-last authors of this work. L.C., D.Z., L.M.P., C.C., M.D.V., and Fe.P. acknowledge European Union's Horizon 2020 Research and Innovation Program under Grant Agreement No. 828972. Fi.P., A.B., and Fe.P. acknowledge European Research Council under the European Union's Horizon 2020 Research and Innovation Program under Grant Agreement No. 677683. Fi.P., M.D.V., and Fe.P. acknowledge European Union's Horizon 2020 Research and Innovation Program under Grant Agreement No. 101016787. M.P. and M.D.V. acknowledge European Research Council under the European Union's Horizon 2020 Research and Innovation Program under Grant Agreement No. 692943. M.P., Fe.P., and M.D.V. acknowledge U.S. National Institutes of Health (Grant No. 1U1FINS108177-01). M.D.V. acknowledges U.S. National Institutes of Health (Grant No. U01NS094190).

Open Access Funding provided by Istituto Italiano di Tecnologia within the CRUI-CARE Agreement.

Conflict of Interest

M.D.V. and Fe.P. are founders and hold private equity in Optogenix, a company that develops, produces, and sells technologies to deliver light into the brain.

Data Availability Statement

The data that support the findings of this study are available from the corresponding author upon reasonable request.

Keywords

nanophotonics, optical fibers, plasmonics, sensing

Received: February 14, 2022

Revised: March 25, 2022

Published online: May 4, 2022

- [1] L. Martín-Moreno, F. J. García-Vidal, H. J. Lezec, K. M. Pellerin, T. Thio, J. B. Pendry, T. W. Ebbesen, *Phys. Rev. Lett.* **2001**, *86*, 1114.
- [2] T. W. Ebbesen, H. J. Lezec, H. F. Ghaemi, T. Thio, P. A. Wolff, *Nature* **1998**, *391*, 667.
- [3] S. Nie, S. R. Emory, *Science* **1997**, *275*, 1102 LP.
- [4] N. Yu, P. Genevet, M. A. Kats, F. Aieta, J.-P. Tetienne, F. Capasso, Z. Gaburro, *Science* **2011**, *334*, 333 LP.
- [5] W. Lu, X. Chen, L. Wang, H. Li, Y. V. Fu, *Anal. Chem.* **2020**, *92*, 6288.
- [6] T. Chung, Y. Lee, M.-S. Ahn, W. Lee, S.-I. Bae, C. S. H. Hwang, K.-H. Jeong, *Nanoscale* **2019**, *11*, 8651.
- [7] Y. Xu, P. Bai, X. Zhou, Y. Akimov, C. E. Png, L.-K. Ang, W. Knoll, L. Wu, *Adv. Opt. Mater.* **2019**, *7*, 1801433.
- [8] Y. Xiong, F. Xu, *Adv. Photonics* **2020**, *2*, <https://doi.org/10.1117/1.ap.2.6.064001>.
- [9] E. Zhao, P. Jia, H. Ebendorff-Heidepriem, H. Li, P. Huang, D. Liu, H. Li, X. Yang, L. Liu, C. Guan, *Nanotechnology* **2017**, *28*, 435504.
- [10] L. Neumann, Y. Pang, A. Houyou, M. L. Juan, R. Gordon, N. F. van Hulst, *Nano Lett.* **2011**, *11*, 355.
- [11] J. Xu, E. Plum, V. Savinov, N. I. Zheludev, *APL Photonics* **2021**, *6*, 036110.
- [12] J. Kwak, W. Lee, J.-B. Kim, S.-I. Bae, K.-H. Jeong, *J. Biomed. Opt.* **2019**, *24*, 1.
- [13] E. J. Smythe, M. D. Dickey, J. Bao, G. M. Whitesides, F. Capasso, *Nano Lett.* **2009**, *9*, 1132.
- [14] M. Principe, M. Consales, A. Micco, A. Crescitelli, G. Castaldi, E. Esposito, V. L. Ferrara, A. Cutolo, V. Galdi, A. Cusano, *Light Sci. Appl.* **2017**, *6*, e16226.
- [15] T. Li, Z. Yu, Z. Wang, Y. Zhu, J. Zhang, *Sensors* **2021**, *21*, 2300.
- [16] A. Ricciardi, M. Consales, G. Quero, A. Crescitelli, E. Esposito, A. Cusano, *ACS Photonics* **2014**, *1*, 69.
- [17] F. Pisano, M. F. Kashif, A. Balena, M. Pisanello, F. De Angelis, L. M. de la Prida, M. Valiente, A. D'Orazio, M. De Vittorio, M. Grande, F. Pisanello, *Adv. Opt. Mater.* **2022**, *10*, 2101649.
- [18] X. He, H. Yi, J. Long, X. Zhou, J. Yang, T. Yang, *Appl. Phys. Lett.* **2016**, *108*, 231105.
- [19] M. Plidschun, H. Ren, J. Kim, R. Förster, S. A. Maier, M. A. Schmidt, *Light Sci. Appl.* **2021**, *10*, 57.
- [20] J. Yang, I. Ghimire, P. C. Wu, S. Gurung, C. Arndt, D. P. Tsai, H. W. H. Lee, *Nanophotonics* **2019**, *8*, 443.
- [21] T. Čižmár, K. Dholakia, *Opt. Express* **2011**, *19*, 18871.
- [22] B. Rahmani, D. Loterie, G. Konstantinou, D. Psaltis, C. Moser, *Light Sci. Appl.* **2018**, *7*, 69.
- [23] I. T. Leite, S. Turtaev, D. E. Boonzajer Flaes, T. Čižmár, *APL Photonics* **2021**, *6*, 036112.
- [24] S. Li, S. A. R. Horsley, T. Tyc, T. Čižmár, D. B. Phillips, *Nat. Commun.* **2021**, *12*, 3751.
- [25] M. Plöschner, B. Straka, K. Dholakia, T. Čižmár, *Opt. Express* **2014**, *22*, 2933.
- [26] I. T. Leite, S. Turtaev, X. Jiang, M. Šiler, A. Cuschieri, P. S. J. Russell, T. Čižmár, *Nat. Photonics* **2018**, *12*, 33.
- [27] M. Plöschner, T. Tyc, T. Čižmár, *Nat. Photonics* **2015**, *9*, 529.
- [28] I. N. Papadopoulos, S. Farahi, C. Moser, D. Psaltis, *Opt. Express* **2012**, *20*, 10583.
- [29] D. Loterie, S. Farahi, I. Papadopoulos, A. Goy, D. Psaltis, C. Moser, *Opt. Express* **2015**, *23*, 23845.
- [30] M. Kang, S.-G. Park, K.-H. Jeong, *Sci. Rep.* **2015**, *5*, 14790.
- [31] L. Collard, F. Pisano, M. Pisanello, A. Balena, M. De Vittorio, F. Pisanello, *APL Photonics* **2021**, *6*, 051301.
- [32] W. Lee, B.-H. Kang, H. Yang, M. Park, J. H. Kwak, T. Chung, Y. Jeong, B. K. Kim, K.-H. Jeong, *Nat. Commun.* **2021**, *12*, 159.
- [33] H. Kang, W. Hong, Y. An, S. Yoo, H.-J. Kwon, Y. Nam, *ACS Nano* **2020**, *14*, 11406.
- [34] S. J. Lee, Y. Chen, B. Lodder, B. L. Sabatini, *Front. Neurosci.* **2019**, *13*, 766.
- [35] M. Jang, Y. Horie, A. Shibukawa, J. Brake, Y. Liu, S. M. Kamali, A. Arbabi, H. Ruan, A. Faraon, C. Yang, *Nat. Photonics* **2018**, *12*, 84.
- [36] F. Pisano, A. Balena, M. F. Kashif, M. Pisanello, G. de Marzo, L. Algieri, A. Qualtieri, L. Sileo, T. Stomeo, A. D'Orazio, M. De Vittorio, F. Pisanello, M. Grande, *Nanotechnology* **2020**, *31*, 435301.
- [37] J. Kwak, W. Lee, J.-B. Kim, S.-I. Bae, K.-H. Jeong, *J. Biomed. Opt.* **2019**, *24*, 1.
- [38] I. Gusachenko, M. Chen, K. Dholakia, *Opt. Express* **2017**, *25*, 13782.
- [39] S. Turtaev, I. T. Leite, T. Altwegg-Boussac, J. M. P. Pakan, N. L. Rochefort, T. Čižmár, *Light Sci. Appl.* **2018**, *7*, 92.
- [40] S. A. Vasquez-Lopez, R. Turcotte, V. Koren, M. Plöschner, Z. Padamsey, M. J. Booth, T. Čižmár, N. J. Emptage, *Light Sci. Appl.* **2018**, *7*, 110.
- [41] R. Di Leonardo, S. Bianchi, *Opt. Express* **2011**, *19*, 247.
- [42] R. Turcotte, C. C. Schmidt, M. J. Booth, N. J. Emptage, *Opt. Lett.* **2020**, *45*, 6599.
- [43] B. M. Silveira, T. Pikálek, M. Stibůrek, P. Ondráčková, P. Jákl, I. T. Leite, T. Čižmár, *Opt. Express* **2021**, *29*, 23083.
- [44] D. Stellinga, D. B. Phillips, S. P. Mekhail, A. Selyem, S. Turtaev, T. Čižmár, M. J. Padgett, *Science* **2021**, *374*, 1395.
- [45] D. Lin, P. Fan, E. Hasman, M. L. Brongersma, *Science* **2014**, *345*, 298 LP.
- [46] P. Pal, A. Bonyár, M. Veres, L. Himics, L. Balázs, L. Juhász, I. Csarnovics, *Sen. Actuators, A* **2020**, *314*, 112225.